Comparative Analysis of Bilateral Permanent Magnet Linear Synchronous Motors With Different Structures

Fengrui Cui, Zhaolong Sun, Wei Xu, *Senior Member, IEEE* , Weichang Zhou, and Yi Liu, *Member, IEEE*

***Abstract*—Permanent magnet linear synchronous motor (PMLSM) has the advantages of high thrust density and good control accuracy, which can be applied in high-power and high-speed occasions. In this paper, the analytical models are established to obtain the electromagnetic performance for the PMLSMs with dual secondaries and dual primaries. The air-gap flux density and the electromagnetic thrust are also obtained by the finite element model to verify theoretical analysis. Besides, an improved structure is also put forward in order to suppress the thrust fluctuation of the PMLSM. Finally, the advantages and disadvantages of two PMLSMs topologies are listed. These analyses would provide a guide for the design of PMLSMs applied in high-power and high-speed occasions.**

***Index Terms*—Bilateral permanent magnet linear synchronous motor (BPMLSM), analytical method, finite element algorithm (FEA), electromagnetic performance.**

I. INTRODUCTION

PERMANENT magnet linear synchronous motors (PMLSM) can directly convert electric energy into linear motion without intermediate motion conversion mechanism. Compared with the traditional way to realize linear motion, such as combination of the rotating motor and rack-pinion or ball-screw, PMSLMs have advantages of direct drive, low loss, excellent dynamic response, simple structure, and so on [1]-[7]. Due to these characteristics aforementioned, PMLSMs can find more applications with requirements of high efficiency, fast response, high accuracy, small volume, *etc*. [8-9]

Recently, many literatures are researched on PMLSMs, which mainly focus on the application of low speed and high precision [5-7]. The analytical method and finite element method are combined to establish the theory of this type of motor, and the corresponding experiments verify its effectiveness. For double-sided PMLSM, it proposes an effective method by shifting the armature or magnetic pole a certain distance to weaken the thrust ripple, and carries out the structure optimization. Based on this optimal design, the electromagnetic and thrust force performances are studied at the no-load and rated load, and validated by prototype measurement [10]. For the cylindrical PMLSM, it studies the magnetic field, back electromotive force (EMF), thrust, armature response, eddy current loss, and optimization design of reducing the positioning force based on the finite element and analytical methods [11].

However, the application range of permanent magnet linear synchronous motors should not be only limited to the application of low speed and high precision. In high-speed and high-power applications, the application prospects of the PMLSM are still very wide. It is necessary to conduct in-depth research on the PMLSM in this application. Therefore, the design and analysis of the moving-magnet-type PMLSM is proposed. The analytical expression of the thrust-density coefficient is derived from basic electromagnetic force laws. Based on the analytical results, the thrust and the thrust ripple are analyzed using the finite element method in different conditions [12]. Besides, two ring windings with novel structures and better performance for the PMLSM is also presented. By comparing the different structures, it finds that the single-layer ring windings are suitable for high-power systems, the double-layer ring windings can be adopted in low fluctuation systems [13].

This paper compares the PMLSMs with different structures in high-speed and high-power situations. According to the analysis of the magnetic field between the motor stator and the mover, two types of bilateral PMLSMs with different structures are proposed. The finite element model and analytical model of the PMLSM are established, and then it analyzes the air gap flux density and thrust of the two motors under no load and load conditions. The finite element analysis model is established by ANSOFT. By comparing the performance of two PMLSMs with different structures, different applications of the two PMLSMs are obtained. Besides, the advantages and disadvantages of two PMLSMs topologies are also listed. Finally, the shape of the permanent magnets of the linear motor is optimized. It concluded that the optimized linear motor has better electromagnetic performance through the finite element simulation, which provides a guide for the selection and optimization design of this type of motor.

Manuscript was submitted for review on 14, December, 2019.

This work has been partly supported in part by National Natural Science Foundation of China under Grants 51877093 and 51707079, in part by the National Key Research and Development Program of China under Grant YS2018YFGH000200, in part by the Key Technical Innovation Program of Hubei Province under Grant 2019AAA026.

Fengrui Cui, Zhaolong Sun and Weichang Zhou are with School of Naval University of Engineering, Wuhan, 430000, China. (e-mail: 1481692056@qq.com, brucesunzl@126.com, 1758414657@qq.com)

Wei Xu (Corresponding Author) and Yi Liu are with the State Key Laboratory of Advanced Electromagnetic Engineering and Technology, School of Electrical and Electronic Engineering, Huazhong University of Science and Technology, Wuhan, 430074, China. (E-mails: weixu@hust.edu.cn, liuyi82@hust.edu.cn)

Digital Object Identifier 10.30941/CESTEMS.2020.00019

II. FINITE ELEMENT MODEL

Figs. 1 and 2 show the two-dimensional finite element models of a 72-slot / 6-pole dual secondary PMLSM (Motor A) and a dual primary PMLSM (Motor B). The mover of PMLSMs is the permanent magnet.

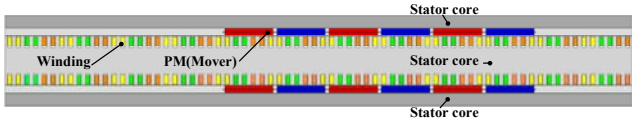

Fig. 1. Double secondary type PMLSM (Motor A).

Fig. 2. Double primary type PMLSM (Motor B).

The common features of PMLSMs includes the stator structure with a core-integrated integer-slot ring winding, a semi-open rectangular slot, and a surface-mounted rectangular radial magnetized permanent magnet substructure, as described in Figs. 1 and 2. The difference between the two types of PMLSM is the mover. Fig. 1 shows a bilateral dynamic magnetic structure with small mass and volume. Each side has an auxiliary stator to close the magnetic circuit and balance the normal force. Fig. 2 uses the form of double primary, and only adopts a structure of a permanent magnet mover. Table I shows the basic parameters of two PMLSMs.

TABLE I
MAIN PARAMETERS OF MOTOR

Parameter	Symbol	Unit	Value
Stator length	L_1	mm	1944
Stator height	H_1	mm	150
Auxiliary stator height	H_3	mm	40
Stator thickness	L_δ	mm	210
Number of slots	Q_1	-	72
Pitch	t_1	mm	27
Tooth width	b_t	mm	13
Slot width	b_0	mm	14
Slot depth	h_0	mm	35
Number of turns in series per phase	N_1	-	24
Number of conductors per slot	Z_1	-	4
The length of the mover	L_2	mm	972
One-sided mover height	H_2	mm	22
The number of poles	$2p$	-	6
Pole distance	τ	mm	162
Permanent magnet length	l_m	mm	210
Permanent magnet width	b_m	mm	150
Permanent magnet height	h_m	mm	10
Aluminum alloy bracket thickness	h_2	mm	2
Air gap length	δ	mm	2
Copper wire gauge	d_1*d_2	mm^2	5.8*1.5
One-sided rated voltage	U	V	380
One-sided rated current	I	A	1341
Synchronous speed	v_s	m/s	37.5
Rated thrust	F	kN	45

Regarding the selection of linear motor materials, DW470-50 is used as the iron core silicon steel sheet of the motor stator, copper flat wire is used for the stator armature winding, and the rare earth permanent magnet material NdFeB is used as the rotor permanent magnet. The material of the bracket is a lighter aluminum alloy plate.

III. ANALYTICAL MODEL

A. Magnetic Field Analysis

For example, in Fig. 1, according to the characteristics of Motor A, a hierarchical analytical model of the motor is established, the Fourier series analysis method and the separated variable method are used to deduce analytical expression for the two-dimensional magnetic field distribution. Finally, the specific distribution of the magnetic field of the linear motor is analyzed with the help of boundary conditions.

Because the motor is a symmetrical structure along the center line of the main stator, in order to simplify the analysis, a 1/2 model below the pole is established, as shown in Fig. 3.

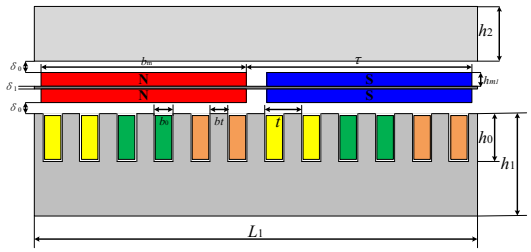

Fig. 3 Motor structure model

In order to facilitate the following analysis and calculation, the simplified structure of the motor is shown in Figure 4. The simplified height of the permanent magnet of the mover h_m is $2h_{m1}$, and the air gap length δ is $\delta_1 + \delta_0/2$.

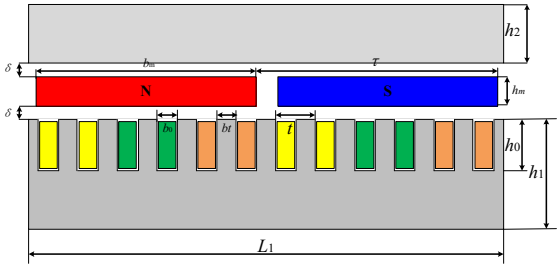

Fig. 4. Simplified motor structure model.

In order to simplify the analysis process, after making the following analysis hypotheses, a multi-gap magnetic field layered analytical model of the motor is established [14], as shown in Fig. 5.

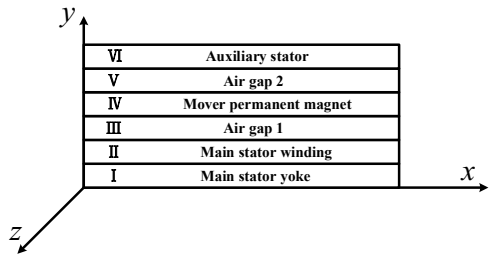

Fig. 5. Hierarchical analytical model of multi-gap magnetic field of motor.

B. Equivalent of Motor Excitation Source

Because the excitation of the motor's magnetic field has two

parts: the stator armature winding and the mover permanent magnet, the two parts should be analyzed independently during the analysis process. The flux density of the internal magnetic field of the motor is analyzed separately when these two parts act independently. After comprehensive consideration, the Equivalent Magnetizing Current (EMC) method was chosen, where the Fourier series was used to represent the stator armature current and the mover [15].

The stator armature winding of Motor A adopts a single-layer short-pitch integer slot winding form, and the number of slots per phase per phase q is 2. Because the stator of the motor is symmetrical, it is possible to analyze the magnetic field distribution generated by only one side of the winding, as shown in Fig. 6.

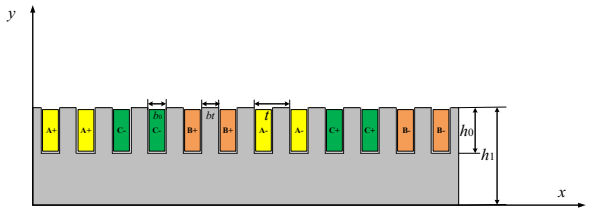

Fig. 6. Schematic diagram of single side toroidal winding.

The main stator of the linear motor adopts a rectangular half-open slot type. The number of turns of the single-layer winding in the slot is N, the slot width is b_0, the slot depth is h_0, and the tooth pitch is t. After the armature currents I_a, I_b, and I_c are entered, the current densities of the three-phase windings in the slot area are

$$\begin{cases} J_a = \dfrac{N \cdot I_a}{h_0 \cdot b_0} \\ J_b = \dfrac{N \cdot I_b}{h_0 \cdot b_0} \\ J_c = \dfrac{N \cdot I_c}{h_0 \cdot b_0} \end{cases}. \tag{1}$$

The current density distribution function of the entire armature winding can be obtained by superposing the expressions of the current density distribution functions of the three-phase windings A, B, and C in the stator armature, and is specifically expressed as

$$J_s(x) = \sum_{k=1,3,5,\cdots}^{\infty} \frac{4}{k\pi} \cos\left(\frac{\pi m}{6} + \frac{b_0}{2}\right) \sin\left(\frac{b_0}{2}\right) \cos\left(\frac{k\pi}{6}\right) \cdot \left[J_a \cos\left(\frac{k\pi x}{\tau} + \frac{k\pi}{6}\right) + J_b \cos\left(\frac{k\pi x}{\tau} - \frac{k\pi}{2}\right) + \ldots \right] \cdot \left[J_c \cos\left(\frac{k\pi x}{\tau} + \frac{5k\pi}{6}\right) \right]. \tag{2}$$

As shown in Fig. 8, it is a waveform diagram of the spatial position of the mover permanent magnet and the corresponding residual magnetization in the PMLSMs. Among them, the pole distance of the mover is x, the width of the mover permanent magnet in the x direction is b_m, the calculated residual magnetic density is B, and the amplitude of the magnetization waveform is M_r.

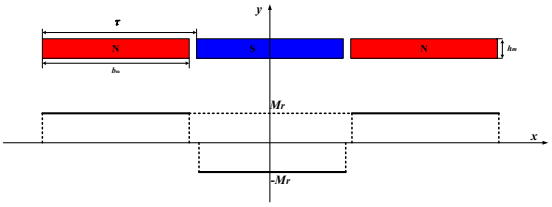

Fig. 7. Remanent magnetization waveform of permanent magnet.

According to the law of Ampere's loop, when the displacement current density is not considered, the current density can be obtained by calculating the curl of the magnetic field strength, in (3). Since the permanent magnets in the motor mover are uniformly magnetized, the surface current density J_m is used to simulate the permanent magnets, and the Fourier series expansion is used to obtain

$$J_m = \nabla \times M_r \tag{3}$$

$$J_m(x) = -\sum_{k=1,3,5,\cdots}^{\infty} \frac{4B_r}{\tau\mu_0} \sin\left(\frac{k\pi b_m}{2\tau}\right) \sin\left(\frac{k\pi x}{\tau}\right). \tag{4}$$

C. Calculation of Motor Magnetic Field

When it solves the armature magnetic field, the excitation effect of the mover is not considered, so that the equivalent body current density of the permanent magnet can be regarded as 0, and the permeability of the permanent magnet in all directions is same as the air permeability rate. The main stator part and the auxiliary stator are ferromagnetic materials, and the magnetic permeability can be regarded as infinite. Therefore, the solution area of the armature magnetic field can be divided into “armature winding” and “air gap + permanent magnet”, which correspond to the two parts II and III + IV + V in Fig. 5. Let the vector magnetic potential of the "armature winding" area of the main stator be $A_{s1}(x, y)$, For the "air gap + permanent magnet" region, the vector magnetic potential is $A_{s2}(x, y)$, which meet the magnetic field equation

$$\begin{cases} \dfrac{\partial^2 A_{s1}(x,y)}{\partial x^2} + \dfrac{\partial^2 A_{s1}(x,y)}{\partial y^2} = -\mu_0 J_s(x,y) \\ \dfrac{\partial^2 A_{s2}(x,y)}{\partial x^2} + \dfrac{\partial^2 A_{s2}(x,y)}{\partial y^2} = 0 \end{cases}. \tag{5}$$

In order to find the partial differential equation in the region, the boundary conditions satisfied by the Poisson equation should be added as follows

$$\begin{cases} \left.\dfrac{\delta A_{s1}}{\delta y}\right|_{y=-(h_m+2\delta+h_0)} = 0 \\ \left.\dfrac{\delta A_{s2}}{\delta y}\right|_{y=0} = 0 \\ \left.\dfrac{\delta A_{s1}}{\delta x}\right|_{y=-(h_m+2\delta)} = \left.\dfrac{\delta A_{s2}}{\delta x}\right|_{y=-(h_m+2\delta)} \\ \left.\dfrac{\delta A_{s1}}{\delta y}\right|_{y=-(h_m+2\delta)} = \left.\dfrac{\delta A_{s2}}{\delta y}\right|_{y=-(h_m+2\delta)} \end{cases}. \tag{6}$$

Combined with the above boundary conditions, the

method of separating variables is used to solve the equations satisfied by the region under the action of the permanent magnet alone, and the expressions of the vector magnetic potential and the corresponding magnetic density of each region are obtained.

For area II these coefficients can be expressed

$$\begin{cases} A_{s1}(x,y)=\sum\limits_{k=1,3,5,\ldots}^{\infty}\left\{\left[\dfrac{4\sqrt{2}NI\tau^2\mu_0}{k^3\pi^3h_0t}\cos\theta_0\cdot\ldots\right.\right. \\ \left.\left.\cos(\dfrac{\pi m}{6}+\dfrac{b_0}{2})\sin(\dfrac{b_0}{2})\cos(\dfrac{k\pi}{6})\right]\cdot\ldots\right\} \\ \left[C_{1k}(e^{\frac{k\pi}{\tau}(2h_m+4\delta+2h_0+y)}+e^{-\frac{k\pi}{\tau}y})-2\right] \\ B_{s1x}(x,y)=\sum\limits_{k=1,3,5,\ldots}^{\infty}\left\{\left[\dfrac{4\sqrt{2}NI\tau^2\mu_0}{k^3\pi^3h_0t}\cos\theta_0\cdot\ldots\right.\right. \\ \left.\left.\cos(\dfrac{\pi m}{6}+\dfrac{b_0}{2})\sin(\dfrac{b_0}{2})\cos(\dfrac{k\pi}{6})\right]\cdot\ldots\right\} \\ C_{1k}(e^{\frac{k\pi}{\tau}(2h_m+4\delta+2h_0+y)}-e^{-\frac{k\pi}{\tau}y}) \\ B_{s1y}(x,y)=\sum\limits_{k=1,3,5,\ldots}^{\infty}\left\{\left[\dfrac{4\sqrt{2}NI\tau^2\mu_0}{k^3\pi^3h_0t}\sin\theta_0\cdot\ldots\right.\right. \\ \left.\left.\cos(\dfrac{\pi m}{6}+\dfrac{b_0}{2})\sin(\dfrac{b_0}{2})\cos(\dfrac{k\pi}{6})\right]\cdot\ldots\right\} \\ \left[2-C_{1k}(e^{\frac{k\pi}{\tau}(2h_m+4\delta+2h_0+y)}+e^{-\frac{k\pi}{\tau}y})\right] \end{cases} . \quad (7)$$

For area III + IV + V these coefficients can be expressed

$$\begin{cases} A_{s2}(x,y)=\sum\limits_{k=1,3,5,\ldots}^{\infty}\left\{\left[\dfrac{4\sqrt{2}NI\tau^2\mu_0}{k^3\pi^3h_0t}\cos\theta_0\cdot\ldots\right.\right. \\ \left.\left.\cos(\dfrac{\pi m}{6}+\dfrac{b_0}{2})\sin(\dfrac{b_0}{2})\cos(\dfrac{k\pi}{6})\right]\cdot\ldots\right\} \\ C_{2k}(e^{\frac{k\pi}{\tau}y}+e^{-\frac{k\pi}{\tau}y}) \\ B_{s2x}(x,y)=\sum\limits_{k=1,3,5,\ldots}^{\infty}\left\{\left[\dfrac{4\sqrt{2}NI\tau^2\mu_0}{k^3\pi^3h_0t}\cos\theta_0\cdot\ldots\right.\right. \\ \left.\left.\cos(\dfrac{\pi m}{6}+\dfrac{b_0}{2})\sin(\dfrac{b_0}{2})\cos(\dfrac{k\pi}{6})\right]\cdot\ldots\right\} \\ C_{2k}(e^{\frac{k\pi}{\tau}y}-e^{-\frac{k\pi}{\tau}y}) \\ B_{s2y}(x,y)=\sum\limits_{k=1,3,5,\ldots}^{\infty}\left\{\left[-\dfrac{4\sqrt{2}NI\tau^2\mu_0}{k^3\pi^3h_0t}\sin\theta_0\cdot\ldots\right.\right. \\ \left.\left.\cos(\dfrac{\pi m}{6}+\dfrac{b_0}{2})\sin(\dfrac{b_0}{2})\cos(\dfrac{k\pi}{6})\right]\cdot\ldots\right\} \\ C_{2k}(e^{\frac{k\pi}{\tau}y}+e^{-\frac{k\pi}{\tau}y}) \end{cases} . \quad (8)$$

These coefficients C_{1k} and C_{2k} can be expressed as

$$\begin{cases} C_{1k}=\dfrac{e^{\frac{k\pi}{\tau}(h_m+2\delta)}-e^{-\frac{k\pi}{\tau}(h_m+2\delta)}}{e^{\frac{2k\pi}{\tau}(h_m+2\delta+h_0)}-1} \\ C_{2k}=\dfrac{e^{\frac{k\pi}{\tau}(h_m+2\delta)}\cdot(1-e^{-\frac{2k\pi}{\tau}h_0})}{e^{\frac{2k\pi}{\tau}(h_m+2\delta+h_0)}-1} \end{cases} . \quad (9)$$

When the permanent magnet magnetic field is solved, the excitation effect of the stator armature is not considered, so that the equivalent body current density of the armature winding can be regarded as 0, and the magnetic permeability in all directions is the same as the air permeability rate. Therefore, the solution area of the permanent magnet magnetic field can be divided into "main stator part + winding + air gap 1", "permanent magnet" and "air gap 2+ auxiliary stator", corresponding to I + II + III, IV in Fig. 5. And V + VI three parts. Set the vector magnetic potential of the sub-main stator section + winding + air gap 1 to $A_{m1}(x, y)$. For the "permanent magnet" region, the vector magnetic potential is $A_{m2}(x, y)$. For the "air gap 2" + Auxiliary stator "area, the vector magnetic position is $A_{m3}(x, y)$, the magnetic field equation and boundary conditions are described as

$$\begin{cases} \dfrac{\partial^2A_{m1}(x,y)}{\partial x^2}+\dfrac{\partial^2A_{m1}(x,y)}{\partial y^2}=0 \\ \dfrac{\partial^2A_{m2}(x,y)}{\partial x^2}+\dfrac{\partial^2A_{m2}(x,y)}{\partial y^2}=-\mu_0J_m(x,y) \\ \dfrac{\partial^2A_{m3}(x,y)}{\partial x^2}+\dfrac{\partial^2A_{m3}(x,y)}{\partial y^2}=0 \end{cases} . \quad (10)$$

$$\begin{cases} \left.\dfrac{\delta A_{m1}}{\delta y}\right|_{y=-(h_m+2\delta)}=0 \\ \left.\dfrac{\delta A_{m3}}{\delta y}\right|_{y=0}=0 \\ \left.\dfrac{\delta A_{m1}}{\delta x}\right|_{y=-(h_m+\delta)}=\left.\dfrac{\delta A_{m2}}{\delta x}\right|_{y=-(h_m+\delta)} \\ \left.\dfrac{\delta A_{m2}}{\delta x}\right|_{y=-\delta}=\left.\dfrac{\delta A_{m3}}{\delta x}\right|_{y=-\delta} \\ \left.\dfrac{\delta A_{m1}}{\delta y}\right|_{y=-(h_m+\delta)}=\left.\dfrac{\delta A_{m2}}{\delta y}\right|_{y=-(h_m+\delta)} \\ \left.\dfrac{\delta A_{m2}}{\delta y}\right|_{y=-\delta}=\left.\dfrac{\delta A_{m3}}{\delta y}\right|_{y=-\delta} \end{cases} . \quad (11)$$

Combined with the above boundary conditions, the method of separating variables is used to solve the equations satisfied by the region under the action of the permanent magnet alone, and the expressions of the vector magnetic potential and the corresponding magnetic density of each region are obtained.

For area I+II+III these coefficients can be expressed

$$\begin{cases} A_{m1}(x,y)=\sum\limits_{k=1,3,5,\ldots}^{\infty}\left\{\dfrac{2\tau B_r}{k^2\pi^2}\sin(\dfrac{k\pi b_m}{2\tau})\sin(\dfrac{k\pi x}{\tau})\cdot\ldots\right. \\ \left.\left[e^{\frac{2k\pi}{\tau}(h_m+2\delta)}\cdot D_{1k}e^{\frac{k\pi}{\tau}y}+D_{1k}e^{-\frac{k\pi}{\tau}y}\right]\right\} \\ B_{m1x}(x,y)=\sum\limits_{k=1,3,5,\ldots}^{\infty}\left\{\dfrac{2B_r}{k\pi}\sin(\dfrac{k\pi b_m}{2\tau})\sin(\dfrac{k\pi x}{\tau})\cdot\ldots\right. \\ \left.\left[e^{\frac{2k\pi}{\tau}(h_m+2\delta)}\cdot D_{1k}e^{\frac{k\pi}{\tau}y}-D_{1k}e^{-\frac{k\pi}{\tau}y}\right]\right\} \\ B_{m1y}(x,y)=\sum\limits_{k=1,3,5,\ldots}^{\infty}\left\{\dfrac{2B_r}{k\pi}\sin(\dfrac{k\pi b_m}{2\tau})\cos(\dfrac{k\pi x}{\tau})\cdot\ldots\right. \\ \left.\left[e^{\frac{2k\pi}{\tau}(h_m+2\delta)}\cdot D_{1k}e^{\frac{k\pi}{\tau}y}+D_{1k}e^{-\frac{k\pi}{\tau}y}\right]\right\} \end{cases} . \quad (12)$$

For area IV these coefficients can be expressed

$$\begin{cases} A_{m2}(x,y)=\sum\limits_{k=1,3,5,\ldots}^{\infty}\left\{\dfrac{2\tau B_r}{k^2\pi^2}\sin(\dfrac{k\pi b_m}{2\tau})\sin(\dfrac{k\pi x}{\tau})\cdot\ldots \left[e^{\frac{k\pi}{\tau}(h_m+2\delta)}\cdot D_{2k}e^{\frac{k\pi}{\tau}y}+D_{2k}e^{-\frac{k\pi}{\tau}y}-2\right]\right\} \\ B_{m2x}(x,y)=\sum\limits_{k=1,3,5,\ldots}^{\infty}\left\{\dfrac{2B_r}{k\pi}\sin(\dfrac{k\pi b_m}{2\tau})\sin(\dfrac{k\pi x}{\tau})\cdot\ldots \left[e^{\frac{k\pi}{\tau}(h_m+2\delta)}\cdot D_{2k}e^{\frac{k\pi}{\tau}y}-D_{2k}e^{-\frac{k\pi}{\tau}y}\right]\right\} \\ B_{m2y}(x,y)=\sum\limits_{k=1,3,5,\ldots}^{\infty}\left\{\dfrac{2B_r}{k\pi}\sin(\dfrac{k\pi b_m}{2\tau})\cos(\dfrac{k\pi x}{\tau})\cdot\ldots \left[e^{\frac{k\pi}{\tau}(h_m+2\delta)}\cdot D_{2k}e^{\frac{k\pi}{\tau}y}+D_{2k}e^{-\frac{k\pi}{\tau}y}-2\right]\right\} \end{cases} \quad (13)$$

For area V+VI these coefficients can be expressed

$$\begin{cases} A_{m3}(x,y)=\sum\limits_{k=1,3,5,\ldots}^{\infty}\left\{\dfrac{2\tau B_r}{k^2\pi^2}\sin(\dfrac{k\pi b_m}{2\tau})\sin(\dfrac{k\pi x}{\tau})\cdot\ldots \left[D_{3k}(e^{\frac{k\pi}{\tau}y}+e^{-\frac{k\pi}{\tau}y})\right]\right\} \\ B_{m3x}(x,y)=\sum\limits_{k=1,3,5,\ldots}^{\infty}\left\{\dfrac{2B_r}{k\pi}\sin(\dfrac{k\pi b_m}{2\tau})\sin(\dfrac{k\pi x}{\tau})\cdot\ldots \left[D_{3k}(e^{\frac{k\pi}{\tau}y}-e^{-\frac{k\pi}{\tau}y})\right]\right\} \\ B_{m3y}(x,y)=\sum\limits_{k=1,3,5,\ldots}^{\infty}\left\{\dfrac{2B_r}{k\pi}\sin(\dfrac{k\pi b_m}{2\tau})\cos(\dfrac{k\pi x}{\tau})\cdot\ldots \left[D_{3k}(e^{\frac{k\pi}{\tau}y}+e^{-\frac{k\pi}{\tau}y})\right]\right\} \end{cases} \quad (14)$$

These coefficients D_{1k}, D_{2k} and D_{3k} can be described by

$$\begin{cases} D_{1k}=\dfrac{e^{-\frac{k\pi}{\tau}(h_m+\delta)}-e^{-\frac{k\pi}{\tau}\delta}}{e^{\frac{k\pi}{\tau}(h_m+2\delta)}-1} \\ D_{2k}=\dfrac{e^{\frac{k\pi}{\tau}\delta}-e^{-\frac{k\pi}{\tau}\delta}}{e^{\frac{k\pi}{\tau}(h_m+2\delta)}-1} \\ D_{3k}=\dfrac{e^{\frac{k\pi}{\tau}\delta}-e^{\frac{k\pi}{\tau}(h_m+\delta)}}{e^{\frac{k\pi}{\tau}(h_m+2\delta)}-1} \end{cases} \quad (15)$$

For the magnetic field analysis of PMLSMs, the main stator of the motor is regarded as a smooth and slotless structure. But in fact, the slotting of the motor will increase the air gap magnetic resistance and reduce the magnetic flux entering the winding. Therefore, the influence of the cogging effect on the magnetic field distribution of the motor should be considered in the analysis. The cogging effect will cause the cogging force generated by the motor magnetic field distortion to be the main component of the positioning force of the motor. The cogging effect thrust fluctuation is also an important factor affecting the motor thrust fluctuation. Therefore, the influence of the cogging structure on the magnetic flux density of the motor is analyzed in detail. The calculated relative permeability distribution function is added to the magnetic field distribution of the stator smooth slotless motor previously analyzed.

When calculating the relative permeability distribution function considering the cogging effect, we first start with a slot model in the cogging area of the main stator. If μ_0 is the vacuum permeability, δ is the air gap length, b_0 is the slot width of a single slot, and t is the tooth pitch. It is supposed $\beta(y)$ to $(B_{max}\text{-}B_{min})/2B_{max}$, the flux density can be obtained by using Schwarz-Christoffel Mapping. The position of the center line of the core tooth reaches the maximum and the position of the slot center line reaches the minimum, so as to obtain the specific expression of $\beta(y)$, as expressed by

$$\beta(y)=\frac{1}{2}\left[1-\frac{1}{\sqrt{1+(\frac{b_0}{2\delta})^2(1+y^2)}}\right]. \quad (16)$$

The air-gap permeability change caused by the cogging effect is added to the magnetic density. The single relative permeability distribution function is

$$\lambda(x,y)=\frac{\lambda'(x,y)}{\frac{\mu_0}{\delta}}=\begin{cases} 1-\left[\dfrac{1}{2}-\dfrac{1}{2\sqrt{1+(\frac{b_0}{2\delta})^2(1+y^2)}}\right]\cdot\ldots \\ \left[1+\cos(\dfrac{\pi x}{0.8b_0})\right] \quad |x|\le 0.8b_0 \\ 1 \qquad 0.8b_0\le|x|\le 0.5t \end{cases} \quad (17)$$

Since the distance of the main stator of the linear motor moving in the x direction is far greater than the air gap length and the tooth width of the motor is about 5 times the air gap length, the relative permeability in the air gap between adjacent tooth slots can be ignored. The effect on the distribution function is the air-gap permeability distribution of the entire linear motor, which is considered to be a periodic function with the tooth pitch t as the period. Fourier series decomposition is performed to obtain the expression (18) of the relative permeability distribution function $\lambda(x,y)$ at y direction in the equivalent air gap of the motor, where b_a is the distance between the centerline of the slot and the axis of the phase a winding.

$$\begin{cases} \lambda(x,y)=a_0+\sum\limits_{n=1}^{\infty}a_n\cos\left[\dfrac{2\pi}{t}n(x+b_a)\right] \\ a_0=1-1.6\dfrac{b_0}{t}\beta(y) \\ a_n=\dfrac{4}{n\pi}\left[\dfrac{1}{2}+\dfrac{(n\frac{b_0}{t})^2}{0.78125-2(n\frac{b_0}{t})^2}\right]\sin(1.6n\pi\dfrac{b_0}{t})\beta(y) \end{cases} \quad (18)$$

From the above analysis, it can be seen that the cogging effect will change with the air gap length δ, awkward width b_0, and tooth pitch t of the PMLSM. When the air gap or tooth pitch increases, the relative permeability distribution function of the

motor also increases, and the effect of the cogging effect gradually decreases. When the slot width b_0 gradually increases, the relative permeability distribution function of the motor follows decreases, the influence of the cogging effect increases at the same time.

Since the area I in Fig. 5 is a mechanical air gap portion between the main stator winding and the mover permanent magnet, it is an important area for the motor to perform energy conversion. In order to examine the accuracy of the above-mentioned analysis of the motor magnetic field, for example, in area II, expression (19) can calculate the magnetic flux density in this area along the y direction.

$$B_y(x,y)=\left[B_{s2y}(x,y)+B_{m1y}(x,y)\right]\cdot\lambda(x,y)\,. \qquad (19)$$

IV. Performance Analysis

A. PMLSM Magnetic Field Analysis

The distribution of the electromagnetic field in a double-sided PMLSM is different under different states. When the motor is in static operation, the magnetic field is only generated by the permanent magnet of the mover. When the stator winding of the motor is passed into a three-phase sinusoidal constant frequency, it can drive the load. Meanwhile, the magnetic field is provided by the stator current winding and the mover permanent magnet. Therefore, the static and transient finite element simulations of the linear motors of each structure were performed, and the distribution diagrams of the magnetic field lines under load conditions is obtained, as shown in Figs 8 and 9.

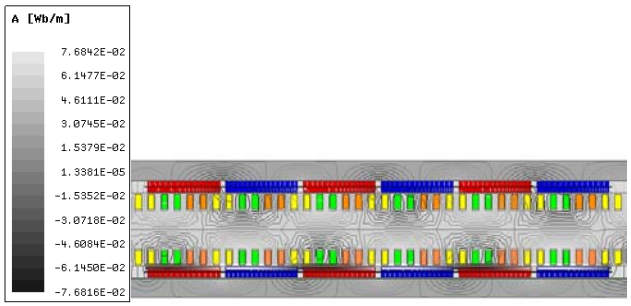

Fig. 8. Magnetic field analysis diagram of motor A.

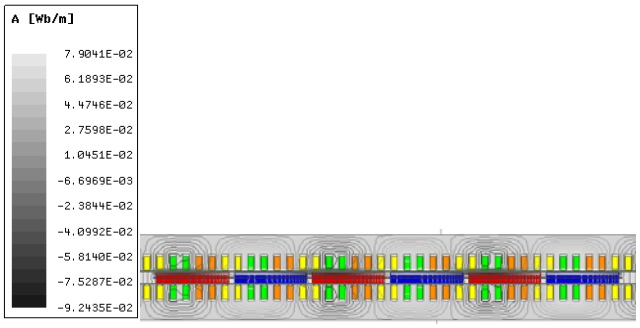

Fig. 9. Magnetic field analysis diagram of motor B.

The quality of the air gap flux density waveform not only affects the back EMF waveform of the permanent magnet linear synchronous motor, but also affects the electromagnetic thrust of the motor. If it obtains a large electromagnetic thrust and increase the thrust density of the motor, the fundamental wave amplitude of the air gap magnetic density must be sufficiently large. A finite element simulation model and an analytical model are established based on the main parameters of the motor obtained in the electromagnetic design mentioned above, and the waveforms and sizes of two different types of PMLSM air-gap flux density are analyzed in detail.

In order to obtain the air-gap flux density waveform distribution of the motor at no load and load, extract the normal component of the motor (the y direction of the model) as shown in Figs. 10 and 11.

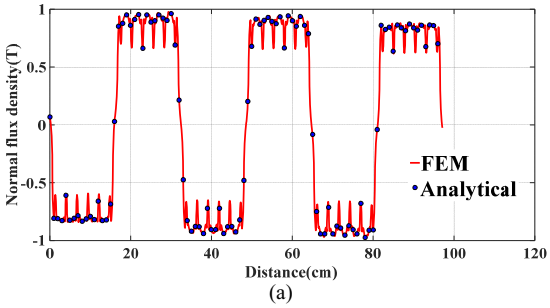

(a)

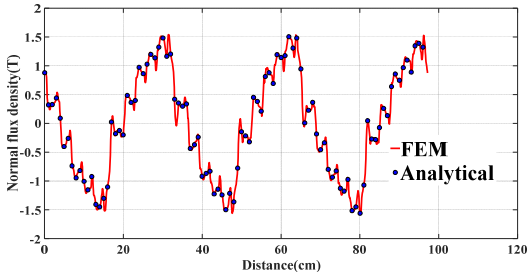

(b)

Fig. 10. Air-gap flux density analysis chart of motor A. (a) Under no load. (b) Under load.

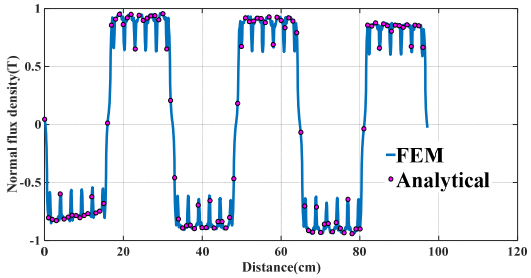

(a)

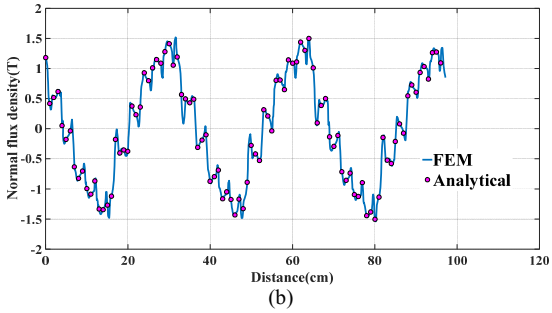

(b)

Fig. 11. Air-gap flux density analysis chart of motor B. (a) Under no load. (b) Under load.

Figs. 10 and 11 shows that the air gap flux density waveforms of the two types of motors are very different under no-load and load conditions. At no load, the air gap magnetic field is approximately sinusoidal, and the waveform has the characteristics of a flat top wave. The normal component of the air gap magnetic density is large, and its amplitude accounts for

80% -90% of the air gap flux density amplitude, mainly affected by the 3rd and 5th harmonics. When the motor is running under load, the air gap flux field also approximates a sinusoidal distribution, the transverse component of the air gap flux honey increases, the proportion of the normal component decreases, and it is greatly affected by harmonics. The difference between the finite element simulation results and the PMLSM air gap flux density analysis results is small, so the accuracy of the method for magnetic field analysis can be proved.

B. PMLSM Electromagnetic Thrust Analysis

In order to examine the electromagnetic performance of the two structures of PMLSMs, three-phase sinusoidal constant-frequency currents I_a, I_b, and I_c are now applied to their stator windings as the excitation source. After the above analysis, it can be known that, through the analytical method and the finite element method (FEM), the air gap flux density error of the two motors under no-load and load conditions is very small. Therefore, in this work, the FEM is used to calculate the electromagnetic force. The electromagnetic thrust of the motor based on FEM is obtained in Fig. 12.

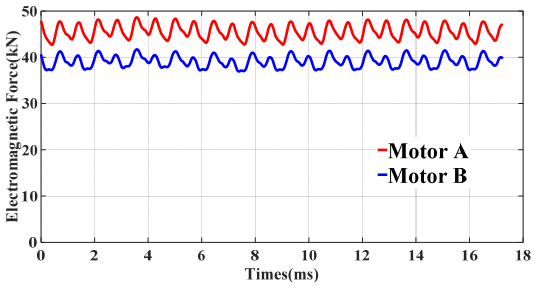

Fig. 12. Thrust curve of PMLSM based on FEM.

Fig. 12 shows the curve of electromagnetic thrust of PMLSMs with two different structures. It can be seen from this figure that the electromagnetic thrust of the two models changes periodically, and the electromagnetic thrust of Motor A is higher than that of Motor B. Among them, the average electromagnetic thrust of Motor A is 45.3178kN and the thrust fluctuation is 17.4%. The average electromagnetic thrust of Motor B is 39.3868kN and the thrust fluctuation is 10.3%. In order to clarify the traits of the two motors, their advantages and disadvantages are summarized in Table II.

Table II
COMPARISON OF ADVANTAGES AND DISADVANTAGES OF TWO MOTORS

Motor	Advantages	Disadvantages
Motor A	High electromagnetic thrust	Large amount of permanent magnets
	The saturation degree of the stator core of Motor is low	Large thrust fluctuation
Motor B	Small amount of permanent magnet	Low electromagnetic thrust
	Small thrust fluctuation	The saturation degree of the stator core of Motor is too high

Both the finite element method and the analytical method are used to solve the air gap flux density of the load, it shows that the air gap flux honey of the two is very similar, but the thrust of the two shows a significant difference. The saturation of the cores of the two types of motor loads can be analyzed, and the flux density of the load can be achieved through finite element calculations. According to the results, it is found that the saturation degree of the stator core of Motor B is too high. It can be concluded that the saturation of the core causes the reduction of its thrust. The characteristics of the two PMLSMs with different structures are very clear. Motor A can produce greater thrust at the same end, while the thrust fluctuations are relatively large, and Motor B has average thrust due to problems such as core saturation. It is smaller than the former with the smaller thrust fluctuation.

V. STRUCTURAL OPTIMIZATION

The vibration and noise of the motor mainly come from electromagnetic vibration, and the stator and rotor parameters and control algorithms of the motor are often optimized from two aspects of motor design and control technology. It is assumed that the stator current is an ideal sine wave, and neglects the influence of core saturation, the thrust fluctuation of the permanent magnet linear synchronous motor mainly comes from the cogging force and the end force. For different thrust fluctuations, different measures can be adopted to reduce its impact. The cogging force is generated by the tangential component of the interaction force between the permanent magnet and the stator teeth.

The shape of the rotor permanent magnet pole arc or the outer surface of the rotor core pole arc is optimized by Exciter pole arc cutting technology, so as to reduce the air gap flux density content and suppress thrust fluctuations. In this paper, take Motor A as an example, as shown in Fig. 13. The air gap flux density generated by the mover permanent magnets of the double-secondary PMLSM is changed by finite element simulation to obtain the hydrogen gap magnetic honeycomb, as shown in Fig. 14. The corresponding electromagnetic thrust is solved, as shown in Fig. 15.

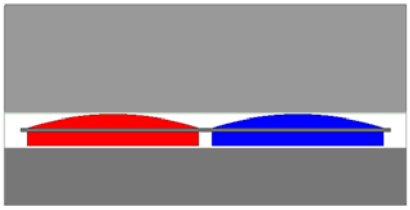

Fig. 13. The structure of Motor A after shaving.

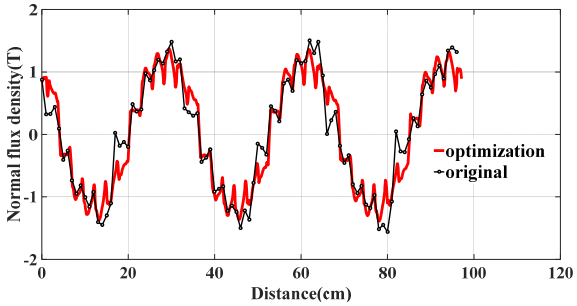

Fig. 14. Air gap magnetic density of PMLSM.

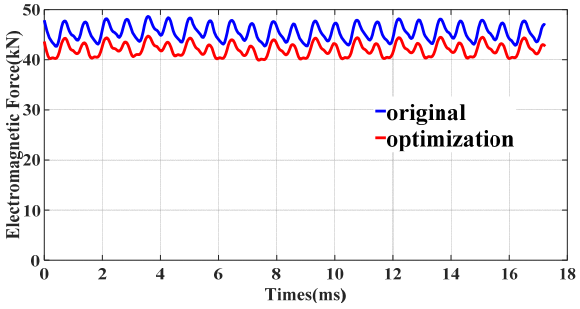

Fig. 15. PLMSM electromagnetic thrust after shaving

Therefore, the finite element model is re-established in ANSOFT. The average value of the electromagnetic thrust with new structure is 43.2431kN, and the thrust fluctuation is 9.1%. Compared with the original structure, the dual-level PMLSM adopting the pole-stripping structure has a slightly lower thrust peak value and less permanent magnet materials. Although the thrust is reduced by 2.0747kN, the thrust fluctuations are decrease by 8.3%. Therefore, this topology can find wide application in industry.

VI. Conclusion

This paper introduces PMLSMs with two different structures, and establishes finite element models and analytical models for two types of motors. The two models were used to analyze the no-load, air-gap magnetic density and average thrust of the two motors. Finally, the two-stage PMLSM's permanent magnet structure was optimized, as the following

1) The motor performance parameters are calculated by the finite element model and the analytical model with little difference, so that it can prove the correctness and effectiveness of the two analysis methods.

2) Motor A has the advantage of large average thrust, but the thrust fluctuation is relatively large. Motor B has a smaller average thrust, but it has the characteristics of small thrust fluctuation and good running stability.

3) After optimizing Motor A for the moving magnet permanent magnet structure, the thrust peak value is slightly reduced, but the material of the permanent magnet material is reduced with the reduced thrust fluctuation about 8.3%.

The analysis of the structure shows that the PMLSM with an optimized permanent magnet structure with a dual-secondaries structure has great advantages in the case of high-power and high-speed motion. This linear motor has broad application prospects.

References

[1] Min S G, Sarlioglu B,"3-D Performance Analysis and Multiobjective Optimization of Coreless-Type PM Linear Synchronous Motors," *IEEE Trans. Ind. Electron.*, vol.65, no.2, pp.1855-1864, Feb.2018.

[2] Chung.S U, Kim J M,"Double-Sided Iron-Core PMLSM Mover Teeth Arrangement Design for Reduction of Detent Force and SpeedRipple," *IEEE Trans. Ind. Electron.*, vol.63, no.5, pp.3000-3008, May 2016.

[3] Hu.H, Zhao J, Liu X, et al,"Magnetic Field and Force Calculation in Linear Permanent-Magnet Synchronous Machines Accounting for Longitudinal End Effect," *IEEE Trans. Ind. Electron.,* vol.63, no.12, pp.7632-7643, Dec.2016.

[4] Pan D, Li L, Wang M,"Modeling and Optimization of Air-core Monopole Linear Motor Based on Multi-physical Fields," *IEEE Trans. Ind. Electron.,* vol.65, no.12, pp.9814-9824, Dec.2018.

[5] Li C, Chen Z, et al. "Integrated coordinated/synchronized contouring control of a Dual-Linear-Motor-Driven Gantry," *IEEE Trans. on Ind. Electron*., DOI.10.1109/TIE.2019.2921287.

[6] He Z, Dong F, Zhao J, et al, "Thrust Ripple Reduction in Permanent Magnet Synchronous Linear Motor Based on Tuned Viscoelastic Damper," *IEEE Trans. Ind. Electron.,* vol.66, no.2, pp.977-987, Feb.2019.

[7] Li C, Li C, Chen Z, et al. "Advanced Synchronization Control of a Dual-Linear-Motor-Driven Gantry with Rotational Dynamics, "*IEEE Trans. on Ind. Electron.*, vol.65, no.9, pp.7526-7535, Sep.2018.

[8] Lu Chen, Kok Kiong Tan, Sunan Huang, et al. "Modeling and compensation of ripples and friction in permanent-magnet linear motor using a hysteretic relay," *IEEE/ASME Transactions on Mechatronics*, vol 15, no.4, pp. 586-594, Aug. 2010.

[9] Ye Yunyue. The theory and application of linear motor Beijing: Machinery Industry Press, pp.1999:102-127(in Chinese).

[10] LU Qinfen, ZHANG Xinmin, HUANG Liren, et al, "Optimal design of shifted type double-sided permanent magnet linear synchronous motors," *Transactions of China Electrotechnical Society*, vol 28, no 11, pp. 35-41, Nov. 2013.

[11] Wang Jiabin, Howe D. "Tubular modular permanent-magnet machines equipped with quasi-halbach magnetized magnets-Part I: Magnetic field distribution, EMF and thrust," *IEEE Trans. on Magnetics.*, vol. 41, no. 9, pp. 2470-2478, Sept. 2005.

[12] LI Liyi, MA Mingna, KOU Baoquan. "Analysis and design of moving-magnet-type linear synchronous motor for electromagnetic launch system," *IEEE Transactions on Plasma Science.*, vol. 39, no. 1, pp. 121-126, Jan. 2011.

[13] ZHANG Zijiao, ZHOU Haibo, DUAN Ji' an. "Design and analysis of a new ring winding structure for permanent magnet linear synchronous motors," *IEEE Transactions on Plasma Science.*, vol. 44, no. 12, pp. 3311-3321, Dec. 2016.

[14] Liu Hao, Bai Chunlan. "Effect of permanent magnets on slotted permanent magnet linear synchronous motor on electromagnetic thrust," *Explosion-proof motors*, vol. 49, no. 2, pp. 5-7, May. 2014.

[15] Gyu-Hong Kang, Jung-Pyo Hong, Gyu-lak kim. "Design and analysis of slotless-type permanent-magnet linear brushless motor by using equivalent magnetizing current," *IEEE Transactions on Industry Applications*., vol. 37, no. 5, pp. 1241-1247, Sept./Oct. 2001.

Fengrui Cui received the B.S. degree in navigation engineering from Naval University of Engineering, Wuhan, China, in 2018. He is currently working toward the M.S. degree in electrical engineering in Naval University of Engineering, Wuhan, China. His research interest is the design for linear motors.

Zhaolong Sun received B.S. and Ph.D. degrees in electrical engineering from the Naval University of Engineering, Wuhan, China, in 2006 and 2011, respectively. In 2013, he joined the Naval University of Engineering, where he is currently an Associate Professor, a Ph.D. Supervisor. His current research interests include electrical devices and machines, especially the design and control for linear motors.

Wei Xu (M'09-SM'13) received the double B.E. and M.E. degrees from Tianjin University, Tianjin, China, in 2002 and 2005, and the Ph.D. from the Institute of Electrical Engineering, Chinese Academy of Sciences, in 2008, respectively, all in electrical engineering.

From 2008 to 2012, he made Postdoctoral Fellow with University of Technology Sydney, Vice Chancellor Research Fellow with Royal Melbourne Institute of Technology, Japan Science Promotion Society Invitation Fellow with Meiji University, respectively. Since 2013, he has been Full Professor with State Key Laboratory of Advanced Electromagnetic Engineering in Huazhong University of Science and Technology, China. He has more than 100 papers accepted or published in IEEE Transactions Journals, two edited books published by Springer Press, one monograph published by China Machine Press, and 120 Invention Patents granted or pending, all in the related fields of electrical machines and drives. He is Fellow of the Institute of Engineering and Technology (IET). He will serve as the General Chair for 2021 International Symposium on Linear Drives for Industry Applications (LDIA 2021) in Wuhan, China. He has served as Associate Editor for several IEEE Transactions Journals, such as IEEE Transactions on Industrial Electronics, and so on.

Weichang Zhou received B.S. and M.S. degree in electrical engineering from Naval University of Engineering, Wuhan, China, in 2016 and 2018, respectively. He is currently pursuing the Ph.D. degree in electrical engineering in Naval University of Engineering, Wuhan China. His research interests include design and application for linear motors.

Yi Liu (M'14) received the B.E. and M.E. degrees in automation and control engineering from the Wuhan University of Science and Technology, Wuhan, China, in 2004 and 2007, respectively, and the Ph.D. degree in mechatronic engineering from the Huazhong University of Science and Technology, Wuhan, China, in 2016.

From 2007 to 2011, he was a Lecturer with the City College, Wuhan University of Science and Technology. From March 2016 to June 2016, he was a Senior R&D Engineer with the Fourth Academy of China Aerospace Science and Industry Group, Wuhan. From July 2016 to October 2019, he was a Postdoctoral Research Fellow at the State Key Laboratory of Advanced Electromagnetic Engineering and Technology, Huazhong University of Science and Technology, where he has been a Lecturer since January 2020. His current research interests include multi-port electrical machines and drive systems.